New Theoretical Model to Describe Carrier Multiplication in Semiconductors Explanation of Disparate Efficiency in $MoTe_2$ versus PbS and PbSe

Weerdenburg, Sven; Singh, Nisha; van der Laan, Marco; Kinge, Sachin; Schall, Peter; Siebbeles, Laurens D.A.

DOI
10.1021/acs.jpcc.4c00383

Publication date
2024

Document Version
Final published version

Published in
Journal of Physical Chemistry C

THE JOURNAL OF PHYSICAL CHEMISTRY C
A JOURNAL OF THE AMERICAN CHEMICAL SOCIETY

pubs.acs.org/JPCC
Article

New Theoretical Model to Describe Carrier Multiplication in Semiconductors: Explanation of Disparate Efficiency in $MoTe_2$ versus PbS and PbSe

Sven Weerdenburg, Nisha Singh, Marco van der Laan, Sachin Kinge, Peter Schall, and Laurens D. A. Siebbeles*

Cite This: J. Phys. Chem. C 2024, 128, 3693−3702

Read Online

ACCESS | Metrics & More | Article Recommendations | Supporting Information

ABSTRACT: We present a theoretical model to compute the efficiency of the generation of two or more electron−hole pairs in a semiconductor by the absorption of one photon via the process of carrier multiplication (CM). The photogeneration quantum yield of electron−hole pairs is calculated from the number of possible CM decay pathways of the electron and the hole. We apply our model to investigate the underlying cause of the high efficiency of CM in bulk 2H−$MoTe_2$, as compared to bulk PbS and PbSe. Electronic band structures were calculated with density functional theory, from which the number of possible CM decay pathways was calculated for all initial electron and hole states that can be produced at a given photon energy. The variation of the number of CM pathways with photon energy reflects the dependence of experimental CM quantum yields on the photon energy and material composition. We quantitatively reproduce experimental CM quantum yields for $MoTe_2$, PbS, and PbSe from the calculated number of CM pathways and one adjustable fit parameter. This parameter is related to the ratio of Coulomb coupling matrix elements and the cooling rate of the electrons and holes. Large variations of this fit parameter result in small changes in the modeled quantum yield for $MoTe_2$, which confirms that its high CM efficiency can be mainly attributed to its extraordinary large number of CM pathways. The methodology of this work can be applied to analyze or predict the CM efficiency of other materials.

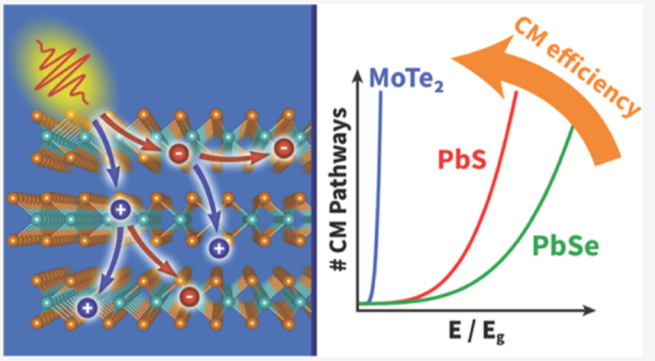

INTRODUCTION

The development of a new generation solar cells requires exploring ways to surpass the Shockley−Queisser limit of 33.7%.[1,2] One of these ways is to enhance the photocurrent of a solar cell via excitation of two or more electrons by the absorption of a single photon.[3] This process of carrier multiplication (CM) can raise the power conversion limit of a single-junction solar cell to 46%.[3,4] Apart from solar cells, CM is also of interest to the development of more efficient photodiodes since it enhances the photocurrent. Note that CM has also been referred to as electron−hole pair multiplication (EHPM) or impaction ionization (II) in bulk semiconductors and has been called multiexciton generation (MEG) in quantum confined systems where excitons are formed rather than free charge carriers.[3,5]

A CM process is schematically shown in Figure 1a. It starts with photoexcitation of a single electron across the band gap of a semiconductor. If the photoexcited electron has sufficient excess energy, exceeding that of the band gap (E_g), it can undergo Coulomb scattering with a valence electron and excite the latter to the conduction band. As depicted in Figure 1b, this leads to the formation of an additional electron−hole pair. Note that the initially photogenerated hole in the valence band can also relax by CM provided its energy is at least $1E_g$ below the top of the valence band, as shown in Figure 1c. Since either the electron or the hole must have an excess energy above E_g, CM is possible for photons with energy above twice the band gap, i.e., $\hbar\omega \geq 2E_g$. In the most ideal case, CM thus has an onset photon energy of $2E_g$ and the number of electron−hole pairs produced per absorbed photon increases with one for each further photon energy increment of E_g.[3] The number of electron−hole pairs produced per absorbed photon, which is known as the electron−hole pair photogeneration quantum yield, then exhibits a steplike dependence on the photon energy. However, photons with energy equal to a multiple of the band gap will, in general, not transfer their entire excess energy to either an electron or a hole.

Received: January 18, 2024
Revised: February 16, 2024
Accepted: February 20, 2024
Published: February 28, 2024

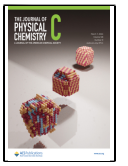

https://doi.org/10.1021/acs.jpcc.4c00383
J. Phys. Chem. C 2024, 128, 3693−3702

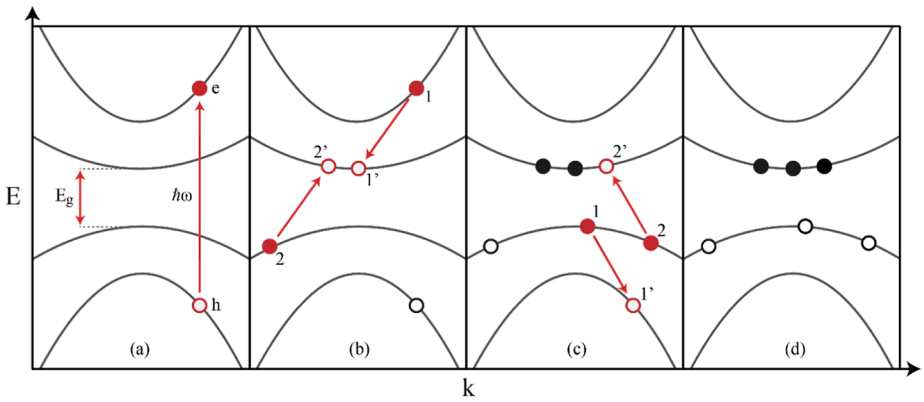

Figure 1. CM is illustrated in a band structure diagram. (a) Photoexcitation of a valence band electron with energy $\hbar\omega$ leads to the generation of an electron−hole pair. In this example, both photogenerated carriers can scatter to yield multiple electron−hole pairs, which is illustrated as a subsequent processes in the following subpanels. (b) The photogenerated electron in state 1 transfers energy to a valence band electron in state 2, resulting in the two final states 1′ and 2′ to be occupied by the electrons. (c) Scattering between two valence band electrons initially in states 1 and 2 results in the relaxation of the electron from state 1 to a lower empty valence band state 1′, this is equivalent to the relaxation of a hole from state 1′ to state 1. The simultaneous excitation of an electron from state 2 to conduction band state 2′ ensures that energy is conserved. (d) The two scattering processes in (b) and (c) finally yield three electron−hole pairs and thus a quantum yield of 3.

In addition, CM occurs in competition with energetic relaxation of electrons and holes by cooling via phonon emission, so that their initial excess energy above the band edges is not fully available for CM. These factors cause the onset energy of CM to be usually larger than twice the band gap and the dependence of the CM quantum yield on photon energy to deviate from the ideal steplike behavior.

CM has been studied for a variety of materials, most notably Pb-chalcogenides,[6−9] Cd-chalcogenides,[10−12] Si nanostructures,[13,14] percolative networks,[4,15] perovskites,[16−19] and transition-metal dichalcogenides (TMDC).[20−22] Particularly, 2H-TMDCs, where the prefix 2H- denotes a trigonal prismatic phase structure, have gained much attention due to reports of a remarkably high efficiency of bulk CM,[20−22] which highly exceeds that of bulk PbS and PbSe.[7] For the 2H−$MoTe_2$ and 2H−WSe_2 TMDCs, the onset energy of CM was found to be close to a photon energy of $2E_g$ and the quantum yield of electron−hole pairs exhibits an almost ideal steplike dependence on photon energy.[20,21] This is very different for bulk PbS and PbSe where the onset energy of CM is as high as $\sim 6E_g$ and the increase of the CM quantum yield with photon energy is much smaller.[7] The origin of the highly efficient CM in these TMDCs has not been rationalized before. A high CM quantum yield requires the rate R_{CM} of CM to be (much) larger than the rate R_{cool} of charge carrier cooling, i.e., their ratio (R_{CM}/R_{cool}) to be large. In the studies on TMDCs mentioned above, the CM rate was estimated to be an order of magnitude larger than the cooling rate.[20,21] A recent theoretical study on TMDCs found that electron−phonon coupling could reduce the band gap upon photoexcitation, which could enable a CM onset even below $2E_g$ and thereby increase the CM efficiency.[23] Furthermore, weak carrier-phonon coupling[24] and long-lived optical phonon modes[25] have been observed in 2H−$MoTe_2$ that could contribute to a low carrier cooling rate. While these are important findings, they do not directly explain why CM in TMDCs is much more efficient than in other bulk materials such as PbS and PbSe.

In this paper, we present a theoretical model that derives the CM efficiency from the number of CM pathways. We apply this model to explain why the experimental CM efficiency of $MoTe_2$[20,21] is much higher than measured for PbS and PbSe.[7] From band structures obtained with density functional theory (DFT), we evaluate all possible Coulomb scattering pathways of photogenerated electrons and holes that lead to the generation of an additional electron−hole pair. The experimental disparate CM quantum yields of $MoTe_2$ versus PbS and PbSe can be described qualitatively based on the very different numbers of CM decay pathways of initially energetic electrons and holes produced by photoexcitation. We quantitatively reproduce the experimental CM quantum yields as a function of photon energy with only one adjustable parameter for each material, which relates to the ratio of the Coulomb interaction strength involved in CM and the charge carrier cooling rate. Our model provides an explanation for the high CM efficiency in $MoTe_2$, as opposed to the much lower CM efficiencies in PbS and PbSe. In our model the Coulomb interaction strength, cooling rate, and optical oscillator strength for photoexcitation were taken to be independent of the electronic states involved. This leads to the conclusion that the variation of the CM rate with photon energy is mainly determined by the number of CM pathways for the decay of electrons and holes. The theoretical framework of this study can be applied to investigate CM efficiencies for other (unexplored) materials.

THEORETICAL METHODS

Electronic Band Structure Calculations. Electronic band structures of $MoTe_2$, PbS, and PbSe were obtained from DFT calculations with the ABINIT package.[26] All calculations were done using optimized norm-conserving Vanderbilt pseudopotentials,[27] a generalized gradient approximation (GGA) exchange−correlation functional,[28] and included spin−orbit coupling. The geometries were based on lattice constants reported literature and are listed in Table S1 in the Supporting Information.[29,30] We used a k-point grid of $n_k = 14 \times 14 \times 7$ crystal momenta for $MoTe_2$ and $n_k = 16 \times 16 \times 16$ for PbS and PbS. The convergence condition between two self-consistent field steps was chosen to be a 10^{-8} hartree (Ha) absolute difference in total energy. Cutoff energies were chosen to be 30, 25, and 40 Ha for $MoTe_2$, PbS, and PbSe, respectively. Band structure diagrams were obtained from k-points along the symmetry lines of the irreducible Brillouin zone, whereas the density of states and the number of CM pathways were

https://doi.org/10.1021/acs.jpcc.4c00383
J. Phys. Chem. C 2024, 128, 3693−3702

computed from k-points in the full Brillouin zone. The conduction bands were shifted using a scissor operator to match the experimentally determined band gaps reported in the literature, which is further discussed below.

Calculation of the Number of Carrier Multiplication Pathways. The number of CM pathways can be obtained by forming sets of charge carrier states and counting each set that fulfills the conditions for an allowed CM pathway. As is shown in Figure 1b, a CM event involves four electronic Bloch states. A primary electron in the initial state with index 1 and energy E_1 decays to a final state 1′ at energy $E_{1'}$. This decay is accompanied by exciting a secondary electron from state 2 with energy E_2 in the valence band to state 2′ with energy $E_{2'}$ in the conduction band. Conservation of energy applies such that $\Delta E_{1',2',1,2} = E_{1'} + E_{2'} - E_1 - E_2 = 0$. Apart from conservation of energy, Coulomb scattering requires the difference of the initial and final crystal momenta $\boldsymbol{k}_i$ of the electrons to be a reciprocal lattice vector $\boldsymbol{G}$, which is zero for Normal-type scattering and nonzero for Umklapp-type scattering.[31,32] The conservation condition of crystal momentum is thus

$$\boldsymbol{k}_{1'} + \boldsymbol{k}_{2'} - \boldsymbol{k}_1 - \boldsymbol{k}_2 = \boldsymbol{G} \tag{1}$$

Furthermore, in the case an electron initiates CM (Figure 1b), the condition $E_{CBM} \leq E_{1'} < E_1$ applies for the primary electron in state 1, where E_{CBM} denotes the minimum energy of the lowest conduction band and E_1 ($E_{1'}$) is the energy of the electron in its initial (final) state. As shown in Figure 1c, CM by relaxation of a hole involves scattering between two valence electrons, where the primary electron 1 remains in the valence band, and thus, the condition $E_{VBM} \geq E_1 > E_{1'}$ must be fulfilled, where E_{VBM} denotes the maximum valence band energy. Finally, the secondary electron in valence band state 2 must be excited to a conduction band state 2′, i.e., $E_2 \leq E_{VBM} < E_{2'}$, which then along with the aforementioned conditions also implies that the energy loss of the primary electron is greater than or equal to the band gap, $E_1 - E_{1'} \geq E_g$.

The conservation of energy and crystal momentum and the conditions for the initial and final states are used to compute the number of CM pathways. The discrete electronic Bloch states obtained from DFT calculations are characterized by a wave vector $\boldsymbol{k}_i$ in the first Brillouin zone, a band index ν_i and an energy E_i (ν_i, $\boldsymbol{k}_i$). By making all possible combinations of the initial and final states of primary and secondary electronic states and assessing the aforementioned conditions, the number of possible CM pathways for any initial primary carrier state can be counted. This leads to the following expression of the number of CM pathways for the initial primary carrier state 1

$$N_{CM}^1 = \frac{1}{2\varepsilon_{tol} {n_k}^2} \sum_{k_2} \sum_{k_{1'}} \sum_{k_{2'}} \sum_{\nu_2} \sum_{\nu_{1'}} \sum_{\nu_{2'}} \delta_{G,k_{1'}+k_{2'}-k_1-k_2} \Theta(\Delta E_{1',2',1,2}, \varepsilon_{tol}) I(E_1, E_{1'}, E_2, E_{2'}) \tag{2}$$

where

$$\Theta(\Delta E_{1',2',1,2}, \varepsilon_{tol}) = \begin{cases} 1 & \text{if } |\Delta E| < \varepsilon_{tol} \\ 0 & \text{if } |\Delta E| \geq \varepsilon_{tol} \end{cases} \tag{3}$$

and

$$I(E_1, E_{1'}, E_2, E_{2'}) = \begin{cases} 1 & \text{if } E_2 \leq E_{VBM} < E_{2'} \text{ and } (E_1 > E_{1'} \geq E_{CBM} \text{ or } E_{VBM} \geq E_1 > E_{1'}) \\ 0 & \text{otherwise} \end{cases} \tag{4}$$

In the summation over initial and final states, the conservation of crystal momentum is taken into account by a Kronecker delta $\delta_{G,\, k1' + k2' - k1 - k2}$. This condition can be satisfied numerically since the DFT calculations provide electronic states on a regular grid of k-points. Conservation of energy of the discrete electronic Bloch states leads to the requirement $\Delta E_{1',2',1,2} = 0$. However, this constraint is too strict since the DFT calculations provide energies on a grid of a finite number of k-points. In addition, consideration of electronic energy only is insufficient since CM can be assisted by absorption or emission of phonons. Therefore, the energy conservation rule is relaxed by using a top-hat function $\Theta(\Delta E, \varepsilon_{tol})$ as defined in eq 3, analogous to previous studies.[33,34] The parameter ε_{tol} relaxes energy conservation over the tolerance interval $2\varepsilon_{tol}$ and the function $\Theta(\Delta E, \varepsilon_{tol})/2\varepsilon_{tol}$ can be considered as a broadened energy conserving Dirac delta function $\delta(\Delta E)$. The function $I(E_1, E_{1'}, E_2, E_{2'})$ defined in eq 4 checks the energy requirements for the initial and final states of the primary and secondary carriers and therefore distinguishes a CM pathway from any ordinary scattering pathway. The summation in eq 2 over all final states at the k-points ($\boldsymbol{k}_{1'}$, $\boldsymbol{k}_{2'}$) scales in a trivial manner with the square of the number of k-points (n_k) included in the DFT calculations. Note that the fourth k-point ($\boldsymbol{k}_2$) is fixed due to conservation of crystal momentum and therefore does not contribute to this scaling factor. Therefore, we divide the summation by ${n_k}^2$, so that for sufficiently large n_k the value of ${N_{CM}}^1$ converges to a constant value and results for different sizes of k-point grids can be directly compared. Hence, for each combination of band indices υ_i in eq 2 the value of ${N_{CM}}^1$ represents the fraction of all ${n_k}^2$ final states 1′ and 2′ per unit energy that can be reached by CM decay of an electron from the initial state with index 1, which excites another electron from the state with index 2. The unit of ${N_{CM}}^1$ is further discussed in the Supporting Information.

Values of N_{CM}^1 were calculated for all initial hole states in the valence bands and electron states in the conduction bands obtained from DFT calculations. In determining the states involved in absorption of a photon with energy $\hbar\omega$ the photon momentum was neglected, so that $\Delta\boldsymbol{k} = 0$ for an optical transition. A constant optical oscillator strength was assumed for all optical transitions. Below, we refer to N_{CM}^1 as the density of the CM pathways.

Modeling the Quantum Yield from the Density of Carrier Multiplication Pathways. Below, we describe our model to obtain the CM quantum yield from the density of CM pathways given by N_{CM}^1 in eq 2. The CM quantum yield is defined as the ratio between the number of generated electron−hole pairs and the number of absorbed photons, i.e.

$$\phi = \frac{N_{EHP}}{N_{photon}} \tag{5}$$

If an incident photon carries at least two band gap multiples of energy ($\hbar\omega \geq 2E_g$), it becomes energetically possible that the photogenerated electron or hole induces CM to yield a second electron−hole pair. At a photon energy of three band gap multiples or more ($\hbar\omega \geq 2E_g$), a primary carrier may have an excess energy above $\geq 2E_g$, so that more CM steps are possible and three or more electron−hole pairs can be produced. Due to computational limitations, these subsequent CM events are not taken into account. Therefore, for photon absorption event i, the quantum yield is determined by the probabilities of CM for the initially photogenerated electron ($P_{CM}^{e_i}$) and hole ($P_{CM}^{h_i}$) only, and can have a value of 1 up to 3, i.e.

https://doi.org/10.1021/acs.jpcc.4c00383
J. Phys. Chem. C 2024, 128, 3693−3702

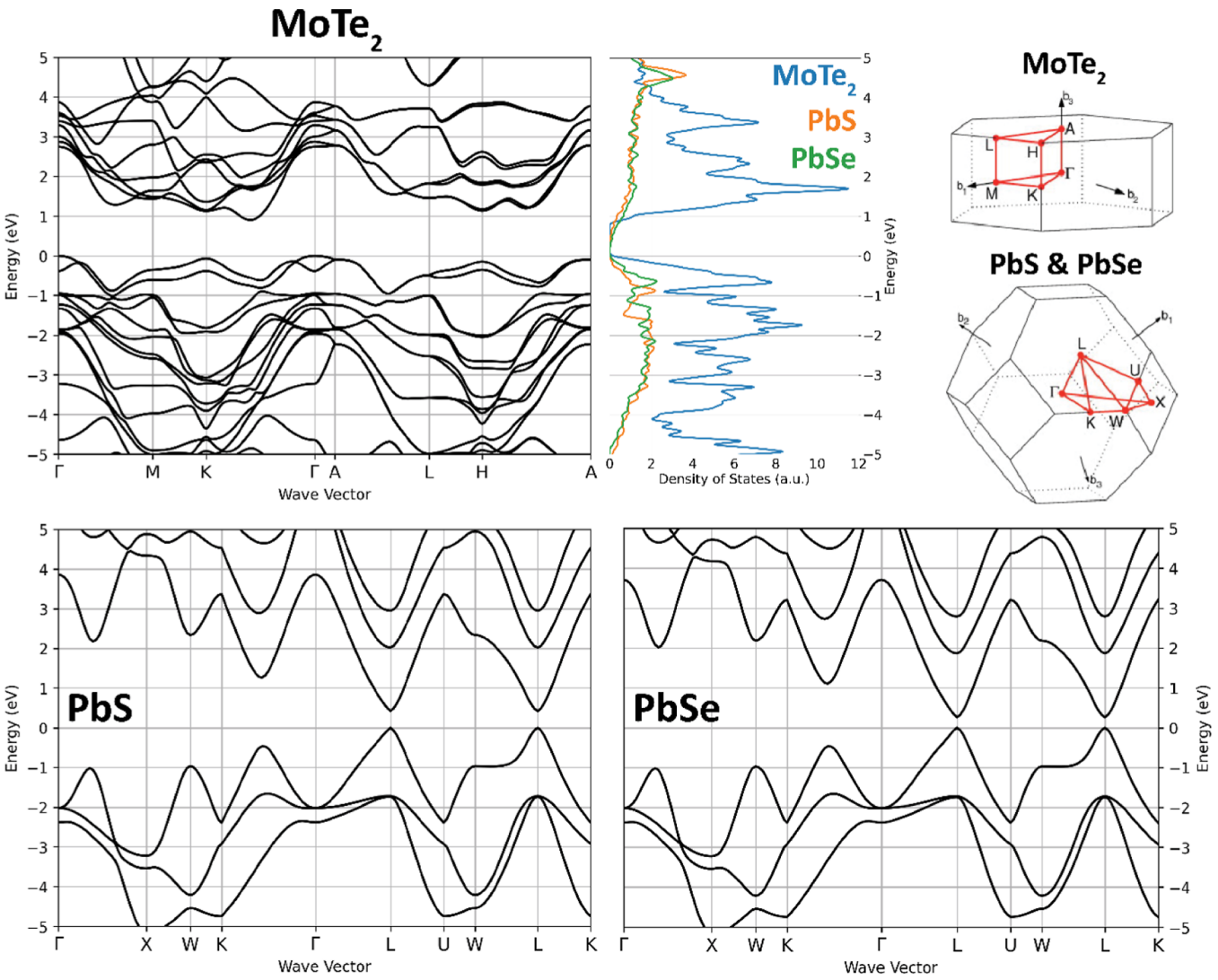

Figure 2. Band structures, density of states, and the Brillouin Zones of 2H−$MoTe_2$, PbS, and PbSe. Brillouin Zone illustrations taken with permission from ref 52. Licensed under a Creative Commons Attribution License.

$$\phi_{e_i,h_i} = 1 + P_{CM}^{e_i} + P_{CM}^{h_i} \tag{6}$$

where e_i and h_i, respectively, denote the conduction and valence band states occupied by the photogenerated primary carriers (electron and hole).

We assume that directly after photoexcitation a generated carrier can follow only one of two paths: (1) it induces CM by Coulomb scattering and yields an additional electron−hole pair or (2) it relaxes by phonon emission without generating an additional electron−hole pair. Carrier cooling is thus modeled as a single step, and a possible sequence of cooling and CM steps is neglected. From these assumptions, the probability of CM for carrier i is then defined as the ratio between the rate of CM and the sum of the CM and carrier cooling rates

$$P_{CM}^{i} = \frac{R_{CM}^{i}}{R_{CM}^{i} + R_{cool}^{i}} \tag{7}$$

where R_{CM}^{i} and R_{cool}^{i} are the total CM and carrier cooling rates, respectively, for a primary carrier in initial state i.

CM rates have been calculated using ab initio and semi-empirical methods for several bulk semiconductors and quantum dots.[7,35−47] In these methods, Fermi's Golden Rule is used, which requires Coulomb matrix elements of all initial and final states. Fortunately, it has been found earlier that the Coulomb matrix elements do not depend much on the electronic states involved in different CM pathways.[38,39,43,44,46−50] Hence, to a good approximation, the Coulomb matrix elements can be kept at a constant value, thereby assuming that each single scattering event occurs at an equal rate. As described in the Supporting Information, the total CM rate for primary carrier in initial state i is then directly proportional to the density of CM decay pathways, N_{CM}^{i}, in eq 2, according to

$$R_{CM}^{i} = F_{CM} N_{CM}^{i} \tag{8}$$

with the prefactor F_{CM} taking into account Coulomb coupling, which is assumed to be independent of the initial and final states. Using eq 8 for the CM rate, the probability of CM in eq 7 can be rearranged to

https://doi.org/10.1021/acs.jpcc.4c00383
J. Phys. Chem. C 2024, 128, 3693−3702

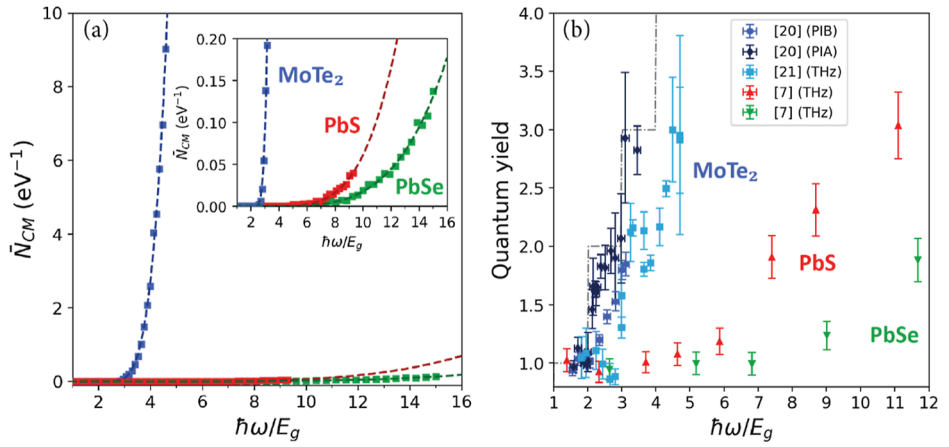

Figure 3. (a) Computed average density of CM pathways, $\bar{N}_{CM} = \bar{N}^{e}_{CM} + \bar{N}^{h}_{CM} = \frac{1}{N_{\hbar\omega}}\sum_{i=1}^{N_{\hbar\omega}}[N^{e_i}_{CM} + N^{h_i}_{CM}]$, in energy intervals of intervals of $\Delta\hbar\omega$ = 0.1 eV for $MoTe_2$, PbS, and PbSe, as a function of band gap multiple. The dashed lines represent the best fit of eq 14 with values of A and P in Table 1. (b) The experimental quantum yield for 2H−$MoTe_2$,[20,21] PbS,[7] and PbSe[7] as a function of band gap multiple.

$$P^{i}_{CM} = \frac{R^{i}_{CM}}{R^{i}_{CM} + R_{cool}} = \frac{N^{i}_{CM}F_{CM}}{N^{i}_{CM}F_{CM} + R_{cool}} = \frac{1}{1 + \left[N^{i}_{CM}\frac{F_{CM}}{R_{cool}}\right]^{-1}} \quad (9)$$

This equation describes the probability of CM for a carrier in the initial state i. The quantum yield for photon absorption event i, that generates the primary initial electron state e_i and hole state h_i is obtained by substitution of eq 9 for the CM probabilities into eq 7, yielding

$$\phi_{e_i,h_i} = 1 + \frac{1}{1 + \left[N^{e_i}_{CM}\frac{F_{CM}}{R_{cool}}\right]^{-1}} + \frac{1}{1 + \left[N^{h_i}_{CM}\frac{F_{CM}}{R_{cool}}\right]^{-1}} \quad (10)$$

A photon with energy $\hbar\omega$ can induce different optical transitions from the valence band to conduction band and thereby can result in the generation of different initial states of a pair of an electron and a hole, e_i and h_i, with different values for $N_{CM}{}^{e_i}$ and $N_{CM}{}^{h_i}$. Assuming a constant optical oscillator strength, the quantum yield at photoexcitation with energy in a small range between $\hbar\omega$ and $\hbar\omega + \Delta\hbar\omega$ is the average quantum yield, $\Phi(\hbar\omega)$, of the total number of possible optical photoexcitations, $N_{\hbar\omega}$, so that

$$\Phi(\hbar\omega) = \frac{1}{N_{\hbar\omega}}\sum_{i=1}^{N_{\hbar\omega}}\phi_{e_i,h_i} \quad (11)$$

Finally, substituting eq 10 into eq 11 results in the CM quantum yield

$$\Phi(\hbar\omega) = 1 + \frac{1}{N_{\hbar\omega}}\sum_{i=1}^{N_{\hbar\omega}}\left[\frac{1}{1 + \left[N^{e_i}_{CM}\frac{F_{CM}}{R_{cool}}\right]^{-1}} + \frac{1}{1 + \left[N^{h_i}_{CM}\frac{F_{CM}}{R_{cool}}\right]^{-1}}\right] \quad (12)$$

As discussed below, we calculate N_{CM} using band structures obtained from DFT and fit eq 12 to experimental quantum yields with F_{CM}/R_{cool} as an adjustable parameter.

The equations above are valid for the physically realistic case of a nonzero cooling rate. However, to obtain insights into the effect of cooling, we also consider the CM quantum yield that would be obtained in absence of cooling, i.e., $R_{cool} \to 0$. In that case, the quantum yield is given by

$$\Phi(\hbar\omega) = 1 + \frac{1}{N_{\hbar\omega}}\sum_{i=1}^{N_{\hbar\omega}}P^{e_i}_{CM} + \frac{1}{N_{\hbar\omega}}\sum_{i=1}^{N_{\hbar\omega}}P^{h_i}_{CM} \quad (13)$$

with $P^{e_i}_{CM} = 1$ if $N^{e_i}_{CM} > 0$, so that CM is possible, and $P^{e_i}_{CM} = 0$ if $N^{e_i}_{CM} = 0$, and analogously for the hole. Hence, the second and third terms in eq 13 are the fractions of the initially photoexcited electrons and holes that decay by the CM, respectively.

RESULTS AND DISCUSSION

Calculated Band Structures and Density of States. The band structures and density of states obtained from the DFT calculations are shown in Figure 2. The calculated band gaps for $MoTe_2$, PbS, and PbSe are 0.72, 0.30, and 0.32 eV, respectively. A scissor operator was applied to match the experimental band gaps of 0.85 eV for $MoTe_2$[20] and 0.42 and 0.26 eV for PbS[51] and PbSe,[51] respectively. It should be noted that Zheng et al. and Kim et al. reported slightly different band gaps for $MoTe_2$, where Kim et al. found an indirect band gap of 0.85 eV and Zheng et al. an excitonic band gap of 0.9 eV.[20,21] This difference may be due to different sample thicknesses, which were 16.4 and 5 nm for Kim et al. and Zheng et al., respectively. Since our calculations were done on bulk 2H−$MoTe_2$, the band gap reported by Kim et al. was used.

https://doi.org/10.1021/acs.jpcc.4c00383
J. Phys. Chem. C 2024, 128, 3693−3702

From the band structures, it is clear that the bands of $MoTe_2$ are relatively flat compared to the more curved bands of the lead chalcogenides. Moreover, $MoTe_2$ has a larger number of bands within the shown energy range, which results in a density of states that is larger than that of the lead chalcogenides. It can also be seen that many of the electronic bands of $MoTe_2$ appear as "bundles", where multiple bands overlap or lie closely together at many values of k. The relatively flat and bundled bands of $MoTe_2$ result in large peaks in the density of states. For PbS and PbSe, at a low photon energy, the excitation occurs around the L-point. Due to the similar curvature of the valence and conduction bands near the L-point, the excess photon energy is divided almost equally over the hole and the electron. As a result, the energy onset of CM is much higher than $2E_g$.

Calculated Density of CM Pathways and Experimental Quantum Yields. The density of CM pathways was computed from eq 2 with energies of the valence and conduction band states from DFT calculations covering the full Brillouin zone. All electronic states that can be generated by photons with energy up to 4 eV were included. Energy conservation was ensured within a range of $\varepsilon_{tol} = 30$ meV in eq 2, which is suitable for the convergence of the results, see the left panel of Figure S1.

Figure 3a shows the summed average density of CM pathways, $\bar{N}_{CM} = \bar{N}_{CM}^{e_i} + \bar{N}_{CM}^{h_i} = \frac{1}{N_{\hbar\omega}} \sum_{i=1}^{N_{\hbar\omega}} [N_{CM}^{e_i} + N_{CM}^{h_i}]$, as a function of the band gap multiple of the photon energy ($\hbar\omega/E_g$). In literature, the rate of impact ionization has been described analytically in the form of $R = A(E - E_0)^P$.[37,39,40,53] We fit the average density of CM pathways similarly, according to

$$\bar{N}_{CM} = A\left(\frac{\hbar\omega}{E_g} - \frac{E_{th}}{E_g}\right)^P \tag{14}$$

where A and P are fitting parameters, and E_{th} is the lowest energy for which we find that $N_{cm} > 0$. The dashed lines in Figure 3a are the results of fits of eq 14 to $\bar{N}_{CM}$. E_{th} and the optimal values of A and P are given in Table 1. The fit reproduces the data for $\bar{N}_{CM}$ very well. It is clear from Figure 3a and the values of A and P that $\bar{N}_{CM}$ increases much more rapidly with photon energy for $MoTe_2$ than for the lead chalcogenides. Figure 3b shows experimental quantum yields obtained from photoinduced bleaching (PIB), intraband absorption (PIA), or terahertz (THz) conductivity measurements.[20,21] Comparing Figure 3a,b shows that the calculated onset of the rise of $\bar{N}_{CM}$ agrees very well with the experimental onsets of CM, which are close to $2.8E_g$ for $MoTe_2$, $5.5E_g$ for PbS, and $7.0E_g$ for PbSe. The calculated trend of the slopes of $\bar{N}_{CM}$ in Figure 3a reflects that of the experimental CM quantum yields in Figure 3b, with the slope drastically decreasing in the order $MoTe_2$, PbS, and PbSe. Hence, the much higher experimental CM quantum yield for $MoTe_2$ can be explained qualitatively by the higher density of CM pathways than for PbS and PbSe.

Table 1. Values of A and B from Fit of eq 14 to the $\bar{N}_{CM}$ Data in Figure 3a

material	A (eV^{-1})	P	E_{th} (eV)	E_{th}/E_g
2H−$MoTe_2$	0.26	4.1	1.9	2.2
PbS	4.6×10^{-5}	3.8	1.4	3.3
PbSe	7.6×10^{-6}	3.9	0.7	2.7

Quantitative Modeling of Experimental Quantum Yields. We used our model outlined above to get insights into the origin of the much higher experimental CM quantum yields reported for $MoTe_2$,[20,21] as compared to PbS and PbSe.[7] We fit eq 12 to the experimental quantum yields with F_{CM}/R_{cool} as the only adjustable parameter. To get insights into the effect of cooling, we also calculated the upper limit of the quantum yield that is reached in the absence of cooling according to eq 13. In the latter case, the quantum yield is solely determined by the presence or absence of at least one CM pathway for each initial state of a carrier.

The experimental CM quantum yields for $MoTe_2$ obtained from transient absorption spectroscopy (PIB and PIA) by Kim et al.[20] and THz conductivity measurements by Zheng et al.[21] are shown in Figure 4a. The quantum yields obtained from PIB are similar to those from the THz conductivity measurements, while PIA gives higher CM quantum yields. The discrepancy between the yields obtained from PIB and THz measurements and those from PIA could be due to a smaller signal-to-noise ratio for the latter, as reflected in the larger error bars for the PIA data. The larger effect of noise for PIA may stem from the fact that the change in transmission during PIA experiments was about 1 order of magnitude smaller than for PIB.[20] The experimental CM quantum yields for PbS and PbSe in Figure 4b,c have been obtained from THz conductivity measurements by Pijpers et al.[7]

The results of fitting eq 12 to experimental quantum yields are shown in Figure 4a,c. The best fit of our model to the experimental data is shown as red dots and the one standard deviation interval as the shaded area. The open diamonds in Figure 4a−c represent the quantum yield calculated in the absence of cooling ($R_{cool} \to 0$) according to eq 13. Figure 4a shows the best fit of our model to the experimental PIB and THz data for $MoTe_2$.[20,21] The fit agrees well with the measured results. Much like the THz data[21] the modeled quantum yield of $MoTe_2$ exhibits a step-like increase near 2.5 eV. The higher CM quantum yields obtained from PIA measurements cannot be reproduced with our model, even in case the maximum quantum yield of CM in the absence of cooling ($R_{cool} \to 0$) is calculated. We therefore did not include the PIA data in our best fit and fitted our model only to the PIB and THz data. As mentioned above, this may be (in part) due to an uncertainty of the PIA data, and it will be of interest to repeat PIA and PIB experiments on $MoTe_2$. Figure 4b,c shows that our model also reproduces the CM quantum yields for PbS and PbSe very well.

Note that in the absence of cooling ($R_{cool} \to 0$) we do not obtain the dashed step-like increase of the quantum yield with photon energy, which implies that only part of all initially photogenerated electrons and holes can decay by CM. This is due to the restrictions of conservation of crystal momentum and energy. Interestingly for $MoTe_2$ the quantum yield without cooling is not much larger than the results from the fit. This means that CM is much faster than cooling in $MoTe_2$, in agreement with the conclusion by Zheng et al. that the rate for the first CM step is nearly an order of magnitude larger than the cooling rate.[21] By contrast, in the absence of cooling, the quantum yields of PbS and PbSe are much higher than those obtained from the best fits; see Figure 4b,c. The latter implies that cooling significantly competes with CM in PbS and PbSe. Figure 2 shows that the electronic bands of $MoTe_2$ are relatively flat compared to the more curved bands of PbS and PbSe. In the case of more flat bands, a change of the k-vector of an electron within a band due to electron−phonon scattering does not

https://doi.org/10.1021/acs.jpcc.4c00383
J. Phys. Chem. C 2024, 128, 3693−3702

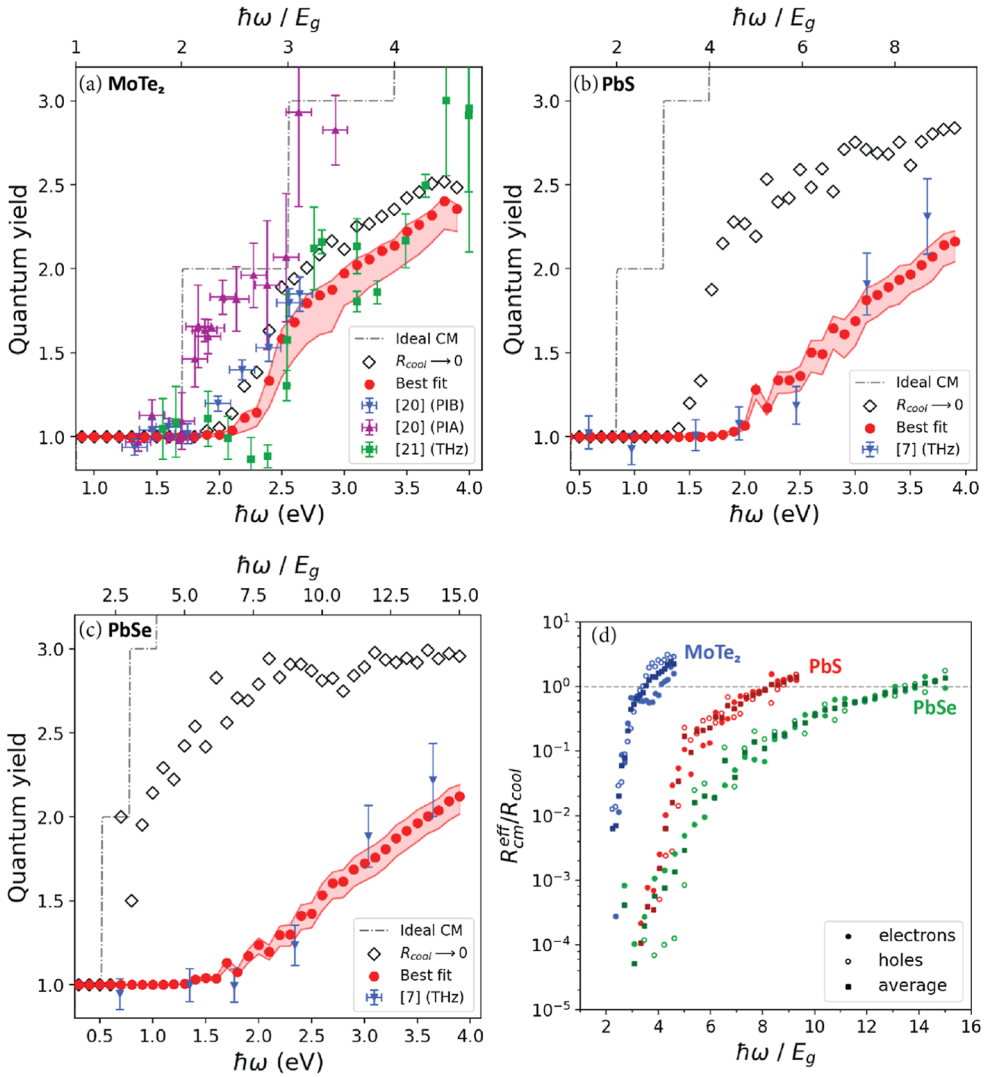

Figure 4. Quantum yields from experiment, best fits of eq 12, and calculated for $R_{cool} \to 0$ according to eq 13 for (a) $MoTe_2$, (b) PbS, and (c) PbSe. The shaded areas represent the one standard deviation interval of the fit, obtained from the variance of the parameter estimate (see SciPy documentation scipy.optimize.curve_fit). The dashed step-like curves illustrate the case of ideal CM. (d) The effective ratio of CM and carrier cooling rates for electrons, holes, and the average of both carriers obtained from eq 15 with the results from fitting eq 12 to the experimental quantum yield. Note that the fluctuations in the calculated quantum yield will in part be due to variations in N_{CM} due to the use of a finite k-point grid, see right panel of Figure S1. This effect is largest at low photon energies, at which only a few optical transitions are possible.

modify its energy much, in contrast to the situation for the more curved bands of PbS and PbSe. As a result, cooling could be slower in $MoTe_2$ and compete less effectively with CM than in the case for PbS and PbSe.

The best fitted values of F_{CM}/R_{cool} are 349 ± 315 eV for $MoTe_2$, 766 ± 393 eV for PbS, and 83.9 ± 28.7 eV for PbSe. The relatively large uncertainty of F_{CM}/R_{cool} of $MoTe_2$ can be attributed to its highly increasing $\bar{N}_{CM}$ as a function of photon energy. As can be seen in Figures S2 and S3, the values of $\bar{N}_{CM}$ for $MoTe_2$ increase so rapidly with photon energy that adjusting F_{CM}/R_{cool} from 1 eV to 10^6 eV has a much smaller impact on the quantum yield than is the case for PbS and PbSe. This therefore leads to a larger uncertainty in the parameter F_{CM}/R_{cool} for $MoTe_2$. Moreover, Figure S2 also shows that the CM efficiency in $MoTe_2$ can predominately be attributed to its large and rapidly increasing number of CM pathways, as large changes in F_{CM}/R_{cool} only slightly affect the quantum yield.

The large uncertainty of F_{CM}/R_{cool} in the materials indicates that quantitative comparison must be done with caution. The large uncertainty of the value of F_{CM}/R_{cool} for $MoTe_2$ makes it unmeaningful to compare it with those of PbS and PbSe. However, the F_{CM}/R_{cool} values of PbS and PbSe do show a significant difference that cannot be attributed solely to the fitting uncertainty and therefore requires further discussion. The value of F_{CM}/R_{cool} of PbSe is smaller than that of PbS because the value of $\bar{N}_{CM}$ is larger in PbSe than in PbS at any given photon energy, whereas the quantum yield of both materials is similar. This is illustrated in Figure S3a,b. Note that the difference between Figures S3 and 3 is the horizontal axis, which is defined as photon energy in eV in Figure S3 rather than band gap multiple $\hbar\omega/E_g$ in Figure 3. Since the value of $\bar{N}_{CM}$ of PbSe is greater than that of PbS while the quantum yields are similar, the F_{CM}/R_{cool} value of PbSe must be lower to compensate for its larger $\bar{N}_{CM}$ value. This implies that PbSe exhibits a larger R_{cool} and/or a smaller F_{CM} than PbS. F_{CM} is inversely proportional to the square of the dielectric function, i.e., $F_{CM} \propto \frac{1}{\varepsilon(q)^2}$.[33,34] The dielectric constants of PbS and PbSe are 169 and 210,

https://doi.org/10.1021/acs.jpcc.4c00383
J. Phys. Chem. C 2024, 128, 3693−3702

respectively.[54] We therefore estimate the F_{CM} value of PbS to be roughly 1.5 times larger than that of PbSe. Details of the physical meaning and unit of F_{CM} are discussed in the Supporting Information. Stewart et al. estimated that the energy-loss rate due to Fröhlich-type electron−phonon coupling is two times larger in PbS than in PbSe, due to a higher longitudinal optical phonon energy and stronger electron−phonon polar coupling.[55] The cooling rate R_{cool} is therefore expected to be twice as large in PbS. The combined estimates of the relative values of F_{CM} and R_{cool} predict that the F_{CM}/R_{cool} of PbS is 1.5/2.0 = 0.75 times that of PbSe, which is clearly in disagreement with our findings.

The cause of the discrepancy between the relative values of F_{CM}/R_{cool} of PbS and PbSe obtained by fitting and the above-mentioned estimation is unclear. As shown in Figure 2, PbS and PbSe have a similar band structure with the main difference being that PbSe has a band gap of 0.26 eV and PbS a band gap of 0.42 eV.[51] The difference in band gap will play a minor role, since the actual CM onset for both is at much higher energy near 2 eV; see Figure S2. Understanding the different fitted values of F_{CM}/R_{cool} for PbS and PbSe asks for calculating F_{CM}, which involves calculating the Coulomb matrix elements with the initial and final state wave functions, and measuring or calculating R_{cool}. This is, however, out of the scope of this work.

From the fitted CM probability, we can back calculate the effective ratio of the CM and cooling rates for electrons and holes separately, with the following expression

$$\frac{R_{CM}^{eff}}{R_{cool}} = \frac{\overline{P}_{CM}}{1 - \overline{P}_{CM}} \tag{15}$$

where $\overline{P}_{CM} = \frac{1}{N_{\hbar\omega}} \sum_{i=1}^{N_{\hbar\omega}} P_{CM}^{i}$, with P_{CM}^{i} describing the probability for CM of an electron in state $i = e_i$, or a hole in state $i = h_i$, see eqs 6 and 7. Note that P_{CM}^{i} depends on the density of CM pathways and this will be reflected in the effective ratio R_{CM}^{eff}/R_{cool}. Figure 4d shows the effective R_{CM}^{eff}/R_{cool} for electrons, holes, and the average R_{CM}^{eff}/R_{cool} of both carriers as a function of band gap multiple. It can be seen that the slope of R_{CM}^{eff}/R_{cool} is steepest for $MoTe_2$, and then, it is steepest for PbS and PbSe, respectively. Equation 15 shows that when the ratio R_{CM}^{eff}/R_{cool} for electrons and holes each reaches unity, $\overline{P}_{CM} = 0.5$ for both, and so the total probability to generate a secondary electron−hole pair is 1, resulting in a total quantum yield of 2. As can be seen from comparing Figure 4a−d, this point is reached at a photon energy of $3.5E_g$ (3.0 eV) for $MoTe_2$, while this occurs at a much higher energy of $8.3E_g$ (3.5 eV) for PbS and at $13.8E_g$ (3.6 eV) for PbSe. This variation of R_{CM}^{eff}/R_{cool} with $\hbar\omega/E_g$ in Figure 4d reflects the trends of the experimental quantum yields in Figure 4a−c. The high CM quantum yield as a function of $\hbar\omega/E_g$ for $MoTe_2$ as compared to PbS and PbSe is thus due to the relatively high density of CM pathways (see Figure 3a), yielding a high CM rate that effectively outcompetes relatively slow cooling.

In addition, Figure 4d shows that R_{CM}^{eff}/R_{cool} for $MoTe_2$ above $3.2E_g$ (2.7 eV) is larger for holes than for electrons. This is caused by a difference in the distribution of the density of the CM pathways, N_{CM}, of the initial electron and hole states. The distribution of N_{CM} for all photogenerated initial states (i.e., all possible combinations of initial electron and hole states at a certain photon energy) is shown in Figure S4. From the upper panel for $MoTe_2$, it can be seen that while the mean value of N_{CM} is typically similar for electrons and holes, above 3 eV the N_{CM} distribution for holes becomes narrower, and the median becomes higher than that of the electrons. This means that at photon energies above 3 eV, a larger fraction of photogenerated holes have a high number of CM pathways than is the case for electrons. This makes CM decay more likely for holes than for electrons above 3 eV. For PbS and PbSe, the N_{CM} distribution is similar for electrons and holes, which leads to comparable CM rates for both carriers.

According to the theoretical analysis above, the high CM efficiency of $MoTe_2$ is mainly due to an extraordinarily high density of CM pathways that goes paired with a beneficial relatively slow cooling rate. These effects can be attributed to the band structure diagram of $MoTe_2$ (Figure 2), which shows a large density of relatively flat bands as opposed to the case of PbS and PbSe. The flatness of the bands of $MoTe_2$ reduces cooling, and their large density results in many CM pathways with conservation of electronic energy and crystal momentum. By contrast, the bands in PbS and PbSe are more curved leading to faster intraband cooling of electrons and holes and the smaller density of states leads to less CM pathways.

CONCLUSIONS

We calculated the density of CM decay pathways, N_{CM}, for the bulk materials 2H−$MoTe_2$, PbS, and PbSe, using electronic band structures from DFT calculations. The variation of N_{CM} with photon energy averaged for electrons and holes, already qualitatively describes the much more efficient CM in 2H−$MoTe_2$, as compared to PbS and PbSe. We take into account cooling of charge carriers in competition with CM, by introducing a fit parameter. In this way, our model quantitatively reproduces the disparate experimental CM quantum yields for the above-mentioned materials in a quantitative manner. The relatively small changes induced by adjusting the fit parameter confirms that the high CM efficiency of 2H−$MoTe_2$ can be mainly attributed to its high density of CM pathways. Our calculations predict a higher probability of CM for holes than for electrons in $MoTe_2$ at photon energies above 3 eV, while these are found to be similar for PbS and PbSe. The theoretical model can be applied to screen new materials for the prospects of efficient CM.

ASSOCIATED CONTENT

Supporting Information

The Supporting Information is available free of charge at https://pubs.acs.org/doi/10.1021/acs.jpcc.4c00383. The code that was used for the calculation of N_{CM}, *cmscript.py*, is available upon reasonable request

> Derivation of eq 8 with definition of the prefactor N_{CM}, discussion of convergence of density of CM decay pathways with the value of energy tolerance ε_{tol} and the number of *k*-points, and box plots showing distributions of density of electron and hole decay pathways as a function of energy (PDF)

AUTHOR INFORMATION

Corresponding Author

Laurens D. A. Siebbeles − *Chemical Engineering Department, Delft University of Technology, Delft 2629 HZ, The Netherlands;* orcid.org/0000-0002-4812-7495; Email: L.D.A.Siebbeles@tudelft.nl

Authors

Sven Weerdenburg − *Chemical Engineering Department, Delft University of Technology, Delft 2629 HZ, The Netherlands*

https://doi.org/10.1021/acs.jpcc.4c00383
J. Phys. Chem. C 2024, 128, 3693−3702

Nisha Singh − *Chemical Engineering Department, Delft University of Technology, Delft 2629 HZ, The Netherlands;* orcid.org/0000-0002-2012-9974

Marco van der Laan − *Institute of Physics, University of Amsterdam, Amsterdam 1098 XH, The Netherlands;* orcid.org/0000-0001-9571-3190

Sachin Kinge − *Materials Research & Development, Toyota Motor Europe, Zaventem B1930, Belgium*

Peter Schall − *Institute of Physics, University of Amsterdam, Amsterdam 1098 XH, The Netherlands;* orcid.org/0000-0003-2612-2762

Complete contact information is available at: https://pubs.acs.org/10.1021/acs.jpcc.4c00383

Author Contributions

The manuscript was written through contributions of all authors. All authors have given approval to the final version of the manuscript.

Notes

The authors declare no competing financial interest.

■ ACKNOWLEDGMENTS

This research received funding from The Netherlands Organization for Scientific Research (NWO) in the framework of the Materials for sustainability and the Ministry of Economic Affairs in the framework of the PPP allowance. The numerical calculations were carried out on the Dutch national e-infrastructure with the support of SURF Cooperative.

■ REFERENCES

(1) Shockley, W.; Queisser, H. J. Detailed Balance Limit of Efficiency of P-n Junction Solar Cells. *J. Appl. Phys.* **1961**, *32* (3), 510−519.

(2) Polman, A.; Knight, M.; Garnett, E. C.; Ehrler, B.; Sinke, W. C. Photovoltaic Materials: Present Efficiencies and Future Challenges. *Science* **2016**, *352* (6283), aad4424.

(3) Maiti, S.; van der Laan, M.; Poonia, D.; Schall, P.; Kinge, S.; Siebbeles, L. D. A. Emergence of New Materials for Exploiting Highly Efficient Carrier Multiplication in Photovoltaics. *Chem. Phys. Rev.* **2020**, *1* (1), 011302.

(4) Kulkarni, A.; Evers, W. H.; Tomić, S.; Beard, M. C.; Vanmaekelbergh, D.; Siebbeles, L. D. A. Efficient Steplike Carrier Multiplication in Percolative Networks of Epitaxially Connected PbSe Nanocrystals. *ACS Nano* **2018**, *12* (1), 378−384.

(5) Beard, M. C.; Midgett, A. G.; Hanna, M. C.; Luther, J. M.; Hughes, B. K.; Nozik, A. J. Comparing Multiple Exciton Generation in Quantum Dots to Impact Ionization in Bulk Semiconductors: Implications for Enhancement of Solar Energy Conversion. *Nano Lett.* **2010**, *10* (8), 3019−3027.

(6) Ellingson, R. J.; Beard, M. C.; Johnson, J. C.; Yu, P.; Micic, O. I.; Nozik, A. J.; Shabaev, A.; Efros, A. L. Highly Efficient Multiple Exciton Generation in Colloidal PbSe and PbS Quantum Dots. *Nano Lett.* **2005**, *5* (5), 865−871.

(7) Pijpers, J. J. H.; Ulbricht, R.; Tielrooij, K. J.; Osherov, A.; Golan, Y.; Delerue, C.; Allan, G.; Bonn, M. Assessment of Carrier-Multiplication Efficiency in Bulk PbSe and PbS. *Nat. Phys.* **2009**, *5* (11), 811−814.

(8) Nair, G.; Geyer, S. M.; Chang, L. Y.; Bawendi, M. G. Carrier Multiplication Yields in PbS and PbSe Nanocrystals Measured by Transient Photoluminescence. *Phys. Rev. B: Condens. Matter Mater. Phys.* **2008**, *78* (12), 125325.

(9) Padilha, L. A.; Stewart, J. T.; Sandberg, R. L.; Bae, W. K.; Koh, W.-K.; Pietryga, J. M.; Klimov, V. I. Aspect Ratio Dependence of Auger Recombination and Carrier Multiplication in PbSe Nanorods. *Nano Lett.* **2013**, *13* (3), 1092−1099.

(10) Cirloganu, C. M.; Padilha, L. A.; Lin, Q.; Makarov, N. S.; Velizhanin, K. A.; Luo, H.; Robel, I.; Pietryga, J. M.; Klimov, V. I. Enhanced Carrier Multiplication in Engineered Quasi-Type-II Quantum Dots. *Nat. Commun.* **2014**, *5* (1), 4148.

(11) Schaller, R. D.; Petruska, M. A.; Klimov, V. I. Effect of Electronic Structure on Carrier Multiplication Efficiency: Comparative Study of PbSe and CdSe Nanocrystals. *Appl. Phys. Lett.* **2005**, *87* (25), 1−3.

(12) Nair, G.; Bawendi, M. G. Carrier Multiplication Yields of CdSe and CdTe Nanocrystals by Transient Photoluminescence Spectroscopy. *Phys. Rev. B: Condens. Matter Mater. Phys.* **2007**, *76* (8), 081304.

(13) Beard, M. C.; Knutsen, K. P.; Yu, P.; Song, Q.; Luther, J.; Ellingson, R.; Nozik, A. J. Multiple Exciton Generation in Silicon Nanocrystals. In *Optics InfoBase Conference Papers*; Optica Publishing Group, 2007; pp 4−10.4

(14) Stolle, C. J.; Lu, X.; Yu, Y.; Schaller, R. D.; Korgel, B. A. Efficient Carrier Multiplication in Colloidal Silicon Nanorods. *Nano Lett.* **2017**, *17* (9), 5580−5586.

(15) Evers, W. H.; Schins, J. M.; Aerts, M.; Kulkarni, A.; Capiod, P.; Berthe, M.; Grandidier, B.; Delerue, C.; van der Zant, H. S. J.; van Overbeek, C.; et al. High Charge Mobility in Two-Dimensional Percolative Networks of PbSe Quantum Dots Connected by Atomic Bonds. *Nat. Commun.* **2015**, *6* (1), 8195.

(16) Cong, M.; Yang, B.; Chen, J.; Hong, F.; Yang, S.; Deng, W.; Han, K. Carrier Multiplication and Hot-Carrier Cooling Dynamics in Quantum-Confined $CsPbI_3$ Perovskite Nanocrystals. *J. Phys. Chem. Lett.* **2020**, *11* (5), 1921−1926.

(17) de Weerd, C.; Gomez, L.; Capretti, A.; Lebrun, D. M.; Matsubara, E.; Lin, J.; Ashida, M.; Spoor, F. C. M.; Siebbeles, L. D. A.; Houtepen, A. J.; et al. Efficient Carrier Multiplication in CsPbI3 Perovskite Nanocrystals. *Nat. Commun.* **2018**, *9* (1), 4199.

(18) Maiti, S.; Ferro, S.; Poonia, D.; Ehrler, B.; Kinge, S.; Siebbeles, L. D. A. Efficient Carrier Multiplication in Low Band Gap Mixed Sn/Pb Halide Perovskites. *J. Phys. Chem. Lett.* **2020**, *11* (15), 6146−6149.

(19) Li, M.; Begum, R.; Fu, J.; Xu, Q.; Koh, T. M.; Veldhuis, S. A.; Grätzel, M.; Mathews, N.; Mhaisalkar, S.; Sum, T. C. Low Threshold and Efficient Multiple Exciton Generation in Halide Perovskite Nanocrystals. *Nat. Commun.* **2018**, *9* (1), 4197.

(20) Kim, J. H.; Bergren, M. R.; Park, J. C.; Adhikari, S.; Lorke, M.; Frauenheim, T.; Choe, D. H.; Kim, B.; Choi, H.; Gregorkiewicz, T.; et al. Carrier Multiplication in van Der Waals Layered Transition Metal Dichalcogenides. *Nat. Commun.* **2019**, *10* (1), 5488.

(21) Zheng, W.; Bonn, M.; Wang, H. I. Photoconductivity Multiplication in Semiconducting Few-Layer MoTe2. *Nano Lett.* **2020**, *20* (8), 5807−5813.

(22) Kim, J. S.; Tran, M. D.; Kim, S. T.; Yoo, D.; Oh, S. H.; Kim, J. H.; Lee, Y. H. Escalated Photocurrent with Excitation Energy in Dual-Gated MoTe2. *Nano Lett.* **2021**, *21* (5), 1976−1981.

(23) Liu, Y.; Frauenheim, T.; Yam, C. Carrier Multiplication in Transition Metal Dichalcogenides Beyond Threshold Limit. *Adv. Sci.* **2022**, *9*, 2203400.

(24) Helmrich, S.; Schneider, R.; Achtstein, A. W.; Arora, A.; Herzog, B.; de Vasconcellos, S. M.; Kolarczik, M.; Schöps, O.; Bratschitsch, R.; Woggon, U.; Owschimikow, N. Exciton-Phonon Coupling in Mono- and Bilayer $MoTe_2$. *2D Mater.* **2018**, *5* (4), 045007.

(25) Li, T.; Zhang, Z.; Zheng, W.; Lv, Y.; Huang, F. A Possible High-Mobility Signal in Bulk MoTe2: Temperature Independent Weak Phonon Decay. *AIP Adv.* **2016**, *6* (11), 115207.

(26) Gonze, X.; Amadon, B.; Antonius, G.; Arnardi, F.; Baguet, L.; Beuken, J. M.; Bieder, J.; Bottin, F.; Bouchet, J.; Bousquet, E.; et al. The Abinit Project: Impact, Environment and Recent Developments. *Comput. Phys. Commun.* **2020**, *248*, 107042.

(27) Hamann, D. R. Optimized Norm-Conserving Vanderbilt Pseudopotentials. *Phys. Rev. B* **2013**, *88* (8), 085117.

(28) Perdew, J. P.; Burke, K.; Ernzerhof, M. Generalized Gradient Approximation Made Simple. *Phys. Rev. Lett.* **1996**, *77* (18), 3865−3868.

(29) Khokhlov, D. *Lead Chalcogenides Physics and Applications*; Optoelectronic Properties of Semiconductors and Superlattices: Taylor & Francis, 1970; Vol. *18*.

(30) Puotinen, D.; Newnham, R. E. The Crystal Structure of MoTe 2. *Acta Crystallogr.* **1961**, *14* (6), 691−692.
(31) Sólyom, J. *Fundamentals of the Physics of Solids*; Springer Berlin, Heidelberg: Budapest, 2002; Vol. *1*.
(32) Lansberg, P. T. *Recombination in Semiconductors*; Cambridge University Press, 2003.
(33) Stobbe, M.; Redmer, R.; Schattke, W. Impact Ionization Rate in GaAs. *Phys. Rev. B* **1994**, *49* (7), 4494−4500.
(34) Sano, N.; Yoshii, A. Impact-Ionization Theory Consistent with a Realistic Band Structure of Silicon. *Phys. Rev. B* **1992**, *45* (8), 4171−4180.
(35) Stobbe, M.; Könies, A.; Redmer, R.; Henk, J.; Schattke, W. Interband Transition Rate in GaAs. *Phys. Rev. B* **1991**, *44* (20), 11105−11110.
(36) Bude, J.; Hess, K. Thresholds of Impact Ionization in Semiconductors. *J. Appl. Phys.* **1992**, *72* (8), 3554−3561.
(37) Kamakura, Y.; Mizuno, H.; Yamaji, M.; Morifuji, M.; Taniguchi, K.; Hamaguchi, C.; Kunikiyo, T.; Takenaka, M. Impact Ionization Model for Full Band Monte Carlo Simulation. *J. Appl. Phys.* **1994**, *75* (7), 3500−3506.
(38) Sano, N.; Yoshii, A. Impact-Ionization Model Consistent with the Band Structure of Semiconductors. *J. Appl. Phys.* **1995**, *77* (5), 2020−2025.
(39) Harrison, D.; Abram, R. A.; Brand, S. Characteristics of Impact Ionization Rates in Direct and Indirect Gap Semiconductors. *J. Appl. Phys.* **1999**, *85* (12), 8186−8192.
(40) Harrison, D.; Abram, R. A.; Brand, S. Impact Ionization Rate Calculations in Wide Band Gap Semiconductors. *J. Appl. Phys.* **1999**, *85* (12), 8178−8185.
(41) Kotani, T.; Van Schilfgaarde, M. Impact Ionization Rates for Si, GaAs, InAs, ZnS, and GaN in the GW Approximation. *Phys. Rev. B: Condens. Matter Mater. Phys.* **2010**, *81* (12), 125201.
(42) Fischetti, M. V.; Sano, N.; Laux, S. E.; Natori, K. Full-Band-Structure Theory of High-Field Transport and Impact Ionization of Electrons and Holes in Ge, Si, and GaAs. *J. Technol. Comput. Aided Des.* **1996**, No. August, 1−50.
(43) Franceschetti, A.; An, J. M.; Zunger, A. Impact Ionization Can Explain Carrier Multiplication in PbSe Quantum Dots. *Nano Lett.* **2006**, *6* (10), 2191−2195.
(44) Rabani, E.; Baer, R. Distribution of Multiexciton Generation Rates in CdSe and InAs Nanocrystals. *Nano Lett.* **2008**, *8* (12), 4488−4492.
(45) Allan, G.; Delerue, C. Role of Impact Ionization in Multiple Exciton Generation in PbSe Nanocrystals. *Phys. Rev. B* **2006**, *73* (20), 205423.
(46) Allan, G.; Delerue, C. Influence of Electronic Structure and Multiexciton Spectral Density on Multiple-Exciton Generation in Semiconductor Nanocrystals: Tight-Binding Calculations. *Phys. Rev. B* **2008**, *77* (12), 125340.
(47) Delerue, C.; Allan, G.; Pijpers, J. J. H.; Bonn, M. Carrier Multiplication in Bulk and Nanocrystalline Semiconductors: Mechanism, Efficiency, and Interest for Solar Cells. *Phys. Rev. B* **2010**, *81* (12), 125306.
(48) Landsberg, P. T.; Robbins, D. J. The First 70 Semiconductor Auger Processes. *Solid State Electron.* **1978**, *21* (11−12), 1289−1294.
(49) Fischetti, M. V.; Sano, N.; Laux, S. E.; Natori, K. Full-Band Monte Carlo Simulation of High-Energy Transport and Impact Ionization of Electrons and Holes in Ge, Si, and GaAs. In *1996 International Conference on Simulation of Semiconductor Processes and Devices. SISPAD '96 (IEEE Cat. No.96TH8095)*; Japan Society of Applied Physics: Tokyo, Japan, 1996; pp 43−44.
(50) Dinh, T. V.; Jungemann, C. Impact Ionization Rates for Strained Si and SiGe. *Solid-State Electron.* **2009**, *53* (12), 1318−1324.
(51) Gibbs, Z. M.; Kim, H.; Wang, H.; White, R. L.; Drymiotis, F.; Kaviany, M.; Jeffrey Snyder, G. Temperature Dependent Band Gap in PbX (X = S, Se, Te). *Appl. Phys. Lett.* **2013**, *103* (26), 262109.
(52) Setyawan, W.; Curtarolo, S. High-Throughput Electronic Band Structure Calculations: Challenges and Tools. *Comput. Mater. Sci.* **2010**, *49* (2), 299−312.
(53) Kunikiyo, T.; Takenaka, M.; Morifuji, M.; Taniguchi, K.; Hamaguchi, C. A Model of Impact Ionization Due to the Primary Hole in Silicon for a Full Band Monte Carlo Simulation. *J. Appl. Phys.* **1996**, *79* (10), 7718−7725.
(54) Madelung, O. *Semiconductors: Data Handbook*; Springer Science & Business Media, 2004.
(55) Stewart, J. T.; Padilha, L. A.; Qazilbash, M. M.; Pietryga, J. M.; Midgett, A. G.; Luther, J. M.; Beard, M. C.; Nozik, A. J.; Klimov, V. I. Comparison of Carrier Multiplication Yields in PbS and PbSe Nanocrystals: The Role of Competing Energy-Loss Processes. *Nano Lett.* **2012**, *12* (2), 622−628.

NOTE ADDED AFTER ASAP PUBLICATION

This Article published ASAP on February 28, 2024. Due to a publication error, equation 2 was missing and the corrected version reposted on March 7, 2024.

https://doi.org/10.1021/acs.jpcc.4c00383
J. Phys. Chem. C 2024, 128, 3693−3702